Solar Phys
DOI 10.1007/s11207-013-0286-8

Chromospheric Sunspot Oscillations in Hα and Ca II 8542 Å

Ram Ajor Maurya · Jongchul Chae · Hyungmin Park · Heesu Yang · Donguk Song · Kyuhyoun Cho

Received: 30 June 2012 / Accepted: 24 March 2013

Abstract We study chromospheric oscillations including umbral flashes and running penumbral waves in a sunspot of active region NOAA 11242 using scanning spectroscopy in Hα and Ca II 8542 Å with the *Fast Imaging Solar Spectrograph* (FISS) at the 1.6 meter *New Solar Telescope* at the Big Bear Solar Observatory. A bisector method is applied to spectral observations to construct chromospheric Doppler-velocity maps. Temporal-sequence analysis of these shows enhanced high-frequency oscillations inside the sunspot umbra in both lines. Their peak frequency gradually decreases outward from the umbra. The oscillation power is found to be associated with magnetic-field strength and inclination, with different relationships in different frequency bands.

Keywords Oscillations, solar · Chromosphere, active · Sunspots, penumbra · Sunspots, umbra · Waves, propagation

1. Introduction

Umbral flashes (UFs) and running penumbral waves (RPWs) are long-known sunspot-oscillation phenomena that have been studied extensively. The first is more three-minute, the latter more five-minute in character.

UFs were first discovered by Beckers and Tallant (1969) in Ca II H and K filtergrams and spectrograms observations of a sunspot. These authors suggested that the UFs may be caused by the magneto-acoustic wave phenomenon. Following a suggestion by Beckers and Tallant (1969), Havnes (1970) theoretically showed that UF brightening occurs in the local umbral gas during the compressional phase of a magneto-acoustic wave; the compression causes a rise in the temperature and a corresponding increase in number density of Ca II atoms. Recently, it has been confirmed by Bard and Carlsson (2010) from NLTE simulations of

Initial Results from FISS
Guest Editor: Jongchul Chae

R.A. Maurya (✉) · J. Chae · H. Park · H. Yang · D. Song · K. Cho
Department of Physics and Astronomy, Seoul National University, Seoul 151-747, Republic of Korea
e-mail: ramajor@astro.snu.ac.kr

Published online: 23 April 2013

the Ca II H line. They concluded that UFs result from increased emission of the local solar material during the passage of acoustic waves originating in the photosphere and steepening to shock in the chromosphere.

RPWs were studied first by Zirin and Stein (1972) and Giovanelli (1972), independently, in Hα filtergrams; they believed the RPWs to be acoustic type and Alfvén type, respectively. A reasonably detailed theory of RPWs in terms of magneto-atmospheric waves was given by Nye and Thomas (1974, 1976). From a simple model of the penumbral atmosphere with a purely horizontal magnetic field, they concluded that the RPWs are gravity-modified fast magneto-acoustic waves that are vertically trapped at the photospheric levels. The waves are more nearly acoustic type at the low levels (convection zone), while they are more nearly of Alfvén type at higher levels (photosphere and low chromosphere). The maximum vertical velocity occurs in the chromosphere, but the density is very low there and most of the wave energy lies in the photosphere and sub-photosphere, where the vertical velocity is lower but the density is much higher.

In recent observations, RPWs appear as a sort of continuation of some of the flash waves. The main difference between the UFs and the RPWs is that the UFs are best seen in Ca II H and K lines, while RPWs are best seen in Hα Dopplergrams. The flashes are present only when the oscillation amplitude is sufficiently large (≥ 5 km s^{-1}), but oscillatory motions are always present in nearly every umbra (Moore, 1981). Furthermore, UFs and RPWs have been interpreted as different manifestations of the same oscillatory phenomenon in a sunspot, combining upward-shock propagation with coherent wave spreading over the entire spot (Zhugzhda and Dzhalilov, 1984; Rouppe van der Voort *et al.*, 2003; Bloomfield, Lagg, and Solanki, 2007).

However, it is still unclear what determines the characteristic properties of the oscillations in sunspot chromospheres. How do the waves that are associated with these oscillations propagate in the magnetized atmosphere? What is the spatial variation of frequency across the sunspot and in features of different spatial scales? The oscillations associated with waves are important to study since they carry some information on the properties of the region from which they originate and through which they propagate. Furthermore, the rapidly evolving field of local helioseismology uses the oscillation properties to investigate the sub-surface structure and dynamics.

UFs and RPWs appear more clearly in Dopplergrams than in intensities. In many earlier studies, the chromospheric oscillations were analyzed by constructing Dopplergrams from filtergrams at fixed wavelengths in the red and blue wings. In this article, simultaneous spectral observations in the Hα and Ca II 8542 Å lines have been used to construct Doppler-velocity maps (hereafter Doppler maps) from the bisectors of these two lines.

The rest of the article is organized as follows: We describe the observational data in Section 2 and present the methods of analysis in Section 3. Results and discussions are given in Section 4. Finally, Section 5 is devoted to the summary and conclusions.

2. Observations

We observed Active Region (AR) NOAA 11242 on 30 June 2011. It was located at heliographic latitude 17°N and longitude 29°W, and consisted of a well-developed sunspot of southern polarity with mean magnetic-field strength 1200 gauss. The sunspot was surrounded by a number of small magnetic fragments of northern polarity. The AR was well observed by the *Fast Imaging Solar Spectrograph* (FISS) instrument (Chae *et al.*, 2012), and the *Helioseismic and Magnetic Imager* (HMI: Schou *et al.*, 2012) onboard the *Solar Dynamics Observatory* (SDO).

FISS is a slit spectrograph taking spectra with a rapid-scan capability. It observes the solar chromosphere simultaneously in two spectral bands centered around the lines Hα and Ca II 8542 Å (hereafter Ca II) with spectral resolutions of 0.045 Å and 0.064 Å, respectively. The pixel resolution at both wavelengths is $\approx 0.16''$ pixel^{-1}.

The FISS data cube, with a field of view of $24''$ of scan width (total number of scans 150) and slit length of $41''$, covers the entire sunspot of AR NOAA 11242. The observations were taken under relatively good seeing conditions during 17:51:38 – 18:55:42 UT, except for a gap during 18:04:45 – 18:18:10 UT, with the scan step sampling, timing, and cadence of 27 seconds, 130 milliseconds, and 30 seconds, respectively, in both spectral bands.

In order to study the association between chromospheric oscillations and magnetic fields, we have used the HMI vector magnetograms: field strength, azimuth angle, and angle of inclination. The angle of inclination is measured from the line-of-sight and azimuth from the $+y$-direction of the heliocentric coordinates (x, y).

3. Data Reduction

Out of 105 cubes for each of Hα and Ca II, seven were discarded, being of low quality due to failure of adaptive optics (AO) locking. The data are processed in two main steps. In the first step, we correct the data for bias, dark, flat, and slit patterns. In the second step the wavelength scales are calibrated. Finally the processed data are compressed using principal component analysis (PCA: Pearson, 1901), which is useful especially when spectral profiles are similar to one another (Rees *et al.*, 2000). PCA compression suppresses the noise to a substantial amount without much loss of information. More details of the processing and PCA compression can be found in Chae *et al.* (2012).

3.1. Alignment

Image rotation at the Coudé focus, telescope guiding errors, errors in slit positioning, and seeing cause shifts between successive scans. We used the far-wing parts of the scans as references. The successive scans were first derotated and then aligned by cross-correlation to the reference scan, and the Hα and Ca II scans were also aligned by cross-correlation. The error due to slit positioning is found to be $\pm 0.16''$. Typical values of the net shifts in scan x- and y-directions were found to be eight pixels and two pixels, respectively. The FISS data were aligned with the HMI images, by manual feature and pattern matching, into solar (x, y) coordinates. Figure 1 shows a mosaic of the aligned FISS and HMI images of AR NOAA 11242 on 30 June 2011.

3.2. Timing Correction

Both the image rotation and the image shifts between successive scans that were corrected by derotation and alignment suggest that the timing per pixel does not have a fixed cadence. We determined the actual observing times per pixel from the alignment vectors.

Figure 2 shows the temporal variation in cadence $[\delta(\Delta t)]$ for three locations (1, 2, and 3, marked with circles in Figure 1b). There is a data gap between 18:04:45 – 18:18:10 UT, and also the images have large shift and rotation. In addition, $\delta(\Delta t)$ varies in the range ± 5 seconds, for a total observation period of 63 minutes. The deviation $\delta(\Delta t)$ for the point 1 (3) becomes more negative (positive) with time, which suggests that the pixel corresponding to this position was observed earlier (later). Note that we have used the data sets starting only from the time 18:18:10 UT, for the oscillation studies. Also, the seven bad-AO scans were excluded.

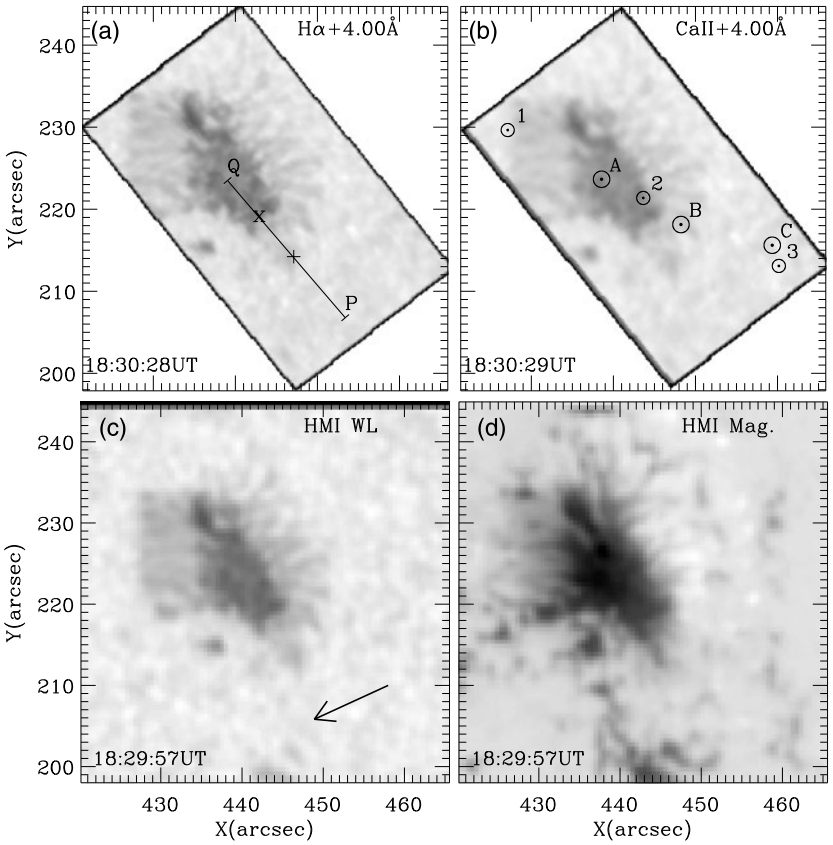

Figure 1 Mosaic of images of AR NOAA 11242 on 30 June 2012 in different wavelengths. The upper panels show the raster images at wavelengths 4.0 Å from Hα (a) and Ca II (b) lines centers. The line PQ (a) marks reference locations for the analysis. The locations marked by the cross (×) and plus (+) symbols represent the approximate boundaries of the umbra and the penumbra, respectively. Small circles labeled with integer numbers (b) mark the locations for which time information is shown in Figure 2, while larger circles labeled with A, B, and C represent three locations as in Figure 4. The lower panels show the HMI continuum (c) and magnetogram (d) images observed near the time of the FISS observation (upper panels). The arrow in panel (c) denotes the direction of the solar disk center.

3.3. Bisector Measurement, Doppler Maps, and Power Maps

We compute the Doppler velocity using the bisectors (Gray, 1976; Dravins, Lindegren, and Nordlund, 1981) of spectral-line profiles. The locus of bisectors represents the asymmetry of the spectral line around the line center. For the bisector for a given spatial location, one may sample the profile asymmetry at a given intensity level (Keil and Yackovich, 1981; Cavallini *et al.*, 1986), at a given separation from the nominal line-center wavelength or the per-pixel measured minimum wavelength (Bhatnagar, Livingston, and Harvey, 1972; von Uexküll, Kneer, and Mattig, 1983; Tziotziou, Tsiropoula, and Mein, 2002; Tziotziou *et al.*, 2007), and lambdameter measurement at given chord length (Slaughter and Wilson, 1972; Stebbins and Goode, 1987). We prefer to measure Doppler velocities with the lambdameter method.

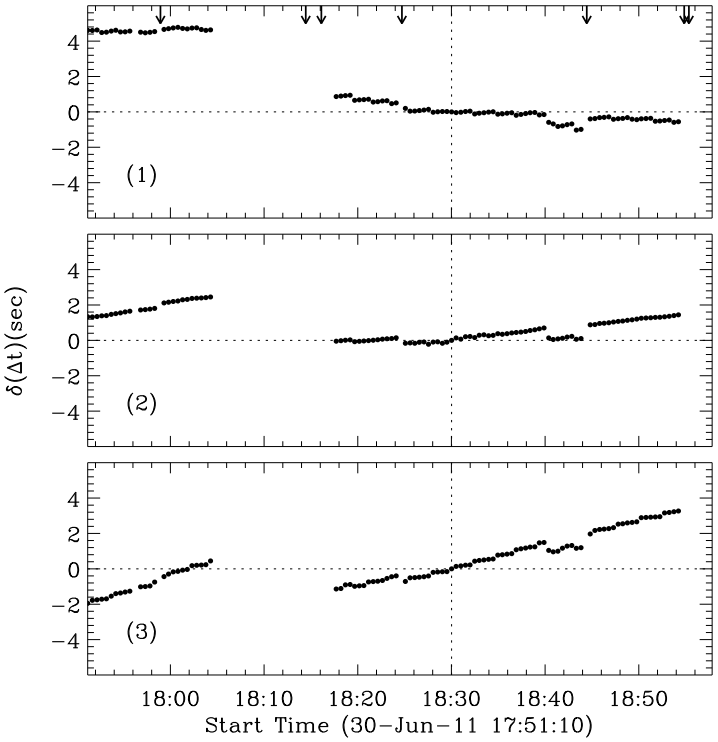

Figure 2 Timing shifts due to image rotation and scanner shifts at the three locations marked in Figure 1b. Vertical dotted line specifies the reference image. Arrows in the upper panel mark the locations of bad-AO scans.

Of course, the lambdameter method has a problem, along with the first two methods, in the case when the Doppler width is changing, *e.g.* spectral lines are wider in the sunspot umbra than in a quiet region. There is a possibility of width variation with time for a given location due to energetic activities. However, it is difficult to remove the width-related variation in the Doppler velocity for every pixel in the time series. To minimize this effect, we have chosen an optimum value of the bisector chord, $\delta\lambda = 0.35$ Å (0.15 Å) for Hα (Ca II). These chords were applied to all the spatial pixels to compute the Doppler maps (see Figure 4, bottom row). To average over remaining image distortions due to seeing, guiding errors, *etc.*, we applied spatial 3×3 boxcar smoothing. For the power analysis of Doppler maps, we prefer not to interpolate the data to equal temporal sampling but instead used the Lomb–Scargle periodogram (LSP) technique (Lomb, 1976; Scargle, 1982).

4. Results and Discussion

Figure 3 shows time-averaged intensity profiles and bisectors of Hα (a) and Ca II (b) lines for location B (see Figure 1b and Figure 4).

The bisectors for the Hα line are "C" shaped while for the Ca II line they are inverse "C", and represent blue and red asymmetry, respectively, in the line profiles. Uitenbroek (2006)

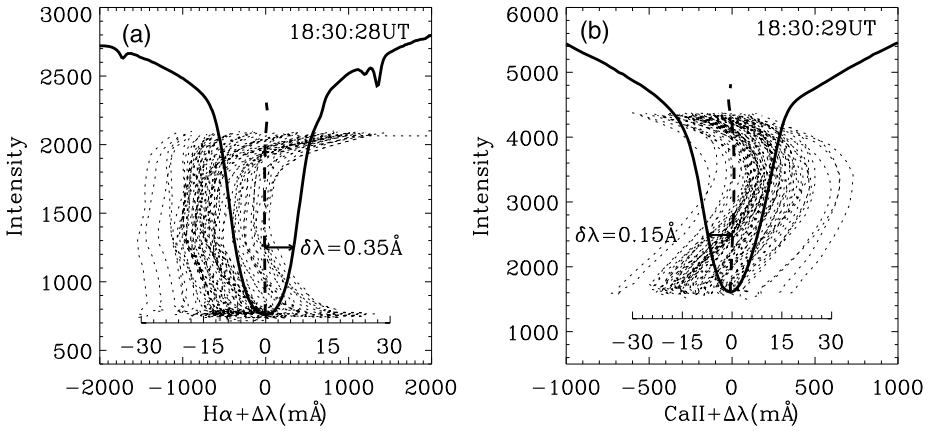

Figure 3 Time-average intensity profiles (thick-solid) and bisectors (thick-dashed) for the location B (see Figure 4). Thin-dashed curves, plotted with respect to x-axes drawn near lines' cores, represent bisectors on a magnified scale (50 times for Hα and 20 times for Ca II) sampled at the same location at different times. The horizontal arrow marks the bisector chord $\delta\lambda = 0.35$ Å (0.15 Å) for Hα (Ca II).

has also reported inverse "C" shaped bisectors and a strong red asymmetry in the Ca II line. The amount of curvature, or, equivalently, the velocity covered by the bisector is a measure of asymmetric flows.

Figure 4 shows samples of chromospheric Doppler maps of the Hα and Ca II lines, respectively, constructed at bisector chords $\delta\lambda = 0.35$ Å and $\delta\lambda = 0.15$ Å. The Doppler velocities in these maps range ± 6 km s^{-1}, where negative/positive velocity shows upward/downward plasma motions. Patterns associated with running penumbral waves, in Hα and Ca II, can be seen in the Doppler maps. The overall red–blue asymmetry of the Doppler maps is caused by off-disk-center viewing. The blue in the limbward part of the penumbra indicates the line-of-sight component of the reverse Evershed flow. It is less evident on the center-side, although filaments there would have better alignment because this spot has no penumbra in the center-side quadrant.

Near the umbra in Ca II, there are pixels with high velocities (marked by an arrow), which are artifacts and occur due to failure of the method adopted for the Doppler-velocity determination. Similar Doppler-velocity and magnetic-field artifacts have been reported previously in measurements obtained from the *Michelson Doppler Imager* (Maurya and Ambastha, 2009; Maurya, 2010) and HMI (Maurya, Vemareddy, and Ambastha, 2012). We found that these pixels are associated with emission features of UFs marked by arrows in the intensity images. This problem was already described by Kneer, Mattig, and von Uexkuell (1981), and also by Tziotziou *et al.* (2006). UF emission features in Ca II can also be seen in Figure 5.

Figure 5 shows the intensity variations in Hα and Ca II lines as a function of time and wavelength for the three spatial locations in umbral, penumbral, and outer-penumbral regions. The Doppler velocities for bisector chords lengths of 0.35 Å (Hα) and 0.15 Å (Ca II) for corresponding positions are over-plotted (dotted curves). For position A, the Ca II line core shows that emission features of UFs and the Doppler velocities computed through bisectors may be inaccurate. Nevertheless, the Doppler velocities for all locations vary quasi-sinusoidally with time which represents the oscillatory motions of the chromospheric plasma emitting the Hα and Ca II lines. There is an interesting pattern of different periods corresponding to different locations. The period of oscillations increases from A to C.

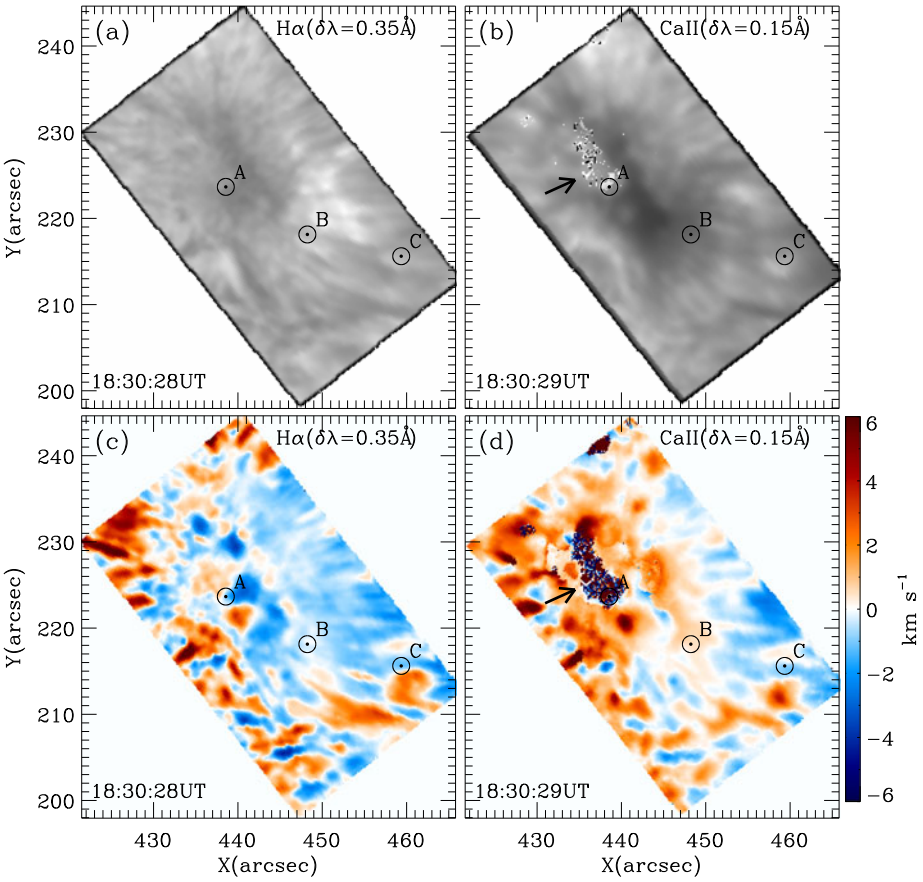

Figure 4 Simultaneous intensity (upper row) and Doppler-velocity (lower row) maps of AR NOAA 11242 computed using the bisector method for the Hα ($\delta\lambda = 0.35$ Å) and Ca II ($\delta\lambda = 0.15$ Å). Arrows mark the umbral locations where Doppler-velocity measurement in Ca II failed due to emission features in the umbral region. The positions A, B, and C, labeled with circles, represent the locations for which wavelength–time maps are shown in Figure 5.

Figure 6 shows space–time intensity maps (upper row) for Hα – 0.35 Å (a) and Ca II – 0.15 Å (b), and Doppler maps (lower row) for the Hα ($\delta\lambda = 0.35$ Å) (c) and Ca II ($\delta\lambda = 0.15$ Å) (d) along the line PQ (see Figure 1a). It is evident that the contrast of the intensity and Doppler-velocity variations in the umbral–penumbral region is large. Also the contrast in Hα is larger than in Ca II. In the umbral region, the ridges are almost vertical and show sinusoidal patterns of intensity and Doppler variations with time. Near the umbral boundary, there is a sharp change in the slope of the ridges. The intensity and Doppler-velocity contrasts in the ridges decay with distance from the umbral boundary to the outer edge of the penumbra, and it is difficult to distinguish intensity ridges further. This shows that the RPWs decay in the super-penumbral regions of the sunspot.

From the raster images, we found that the amplitude of RPWs gradually decreases away from the line centers. It is difficult to identify the RPWs beyond the 0.75 Å in the Hα and 0.50 Å in the Ca II. Also, the amplitude of RPWs decreases from the umbral boundary to the

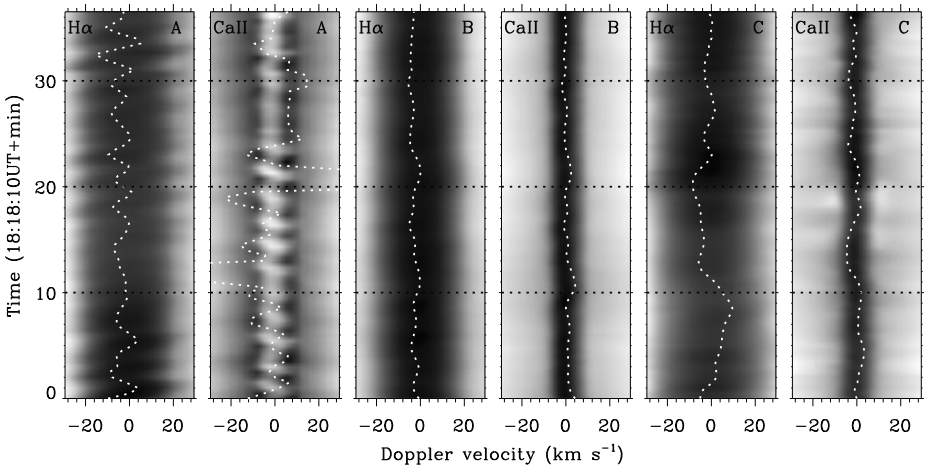

Figure 5 Intensity as a function of wavelength and time for Hα (panels, first, third, and fifth from the left) and Ca II (panels, second, fourth and sixth from the left) at three spatial locations [A, B, and C] respectively for the umbra, penumbra, and super-penumbra (see Figure 4). Dotted curves, passing through the lines' centers, show the Doppler velocities (magnified by factor of five for all of the panels except panel 2 from the left) at corresponding locations.

outer edge of the penumbra, which is consistent with the earlier reports (Giovanelli, 1972; Zirin and Stein, 1972).

The space–time Doppler panels of Figure 6 show that the RPWs have much more blue than red in Hα, the reverse in Ca II but no such asymmetry appears in Tziotziou *et al.* (2006, 2007). However, their traces also have larger amplitude for Ca II in the umbra and a shift between largely negative for Hα and largely positive for Ca II.

Figure 7 shows a sample of oscillation-power maps, for the Hα ($\delta\lambda = 0.35$ Å) (upper) and Ca II ($\delta\lambda = 0.15$ Å) (lower), averaged over different frequency bands. For comparison, all the maps are shown in the same amplitude range. It is evident that there is more power in the sunspot umbra at higher frequency band ($4.5 \leq \nu < 7.5$ mHz) than the lower-frequency band ($1.5 \leq \nu < 4.5$ mHz), while in the outer penumbra the power is higher at lower frequencies than at higher frequencies. This is consistent with earlier reports: *e.g.* Rouppe van der Voort *et al.* (2003). This pattern exists in both the spectral bands. The high-frequency oscillations in Ca II are found to be concentrated in smaller regions than in Hα, although there are some bad data points in the umbra of Ca II maps due to artifacts in the Doppler-velocity images (*cf.* Figure 4).

Figure 8 shows the oscillation power as a function of distance (along the line PQ in Figure 1a) and frequency. There is a clear linear trend in the maximum-power variation from the umbra to outward. The oscillations in the three- and five-minute bands, along with the features at other frequencies, can be seen in both maps.

In order to study the nature of the waves in the sunspot, we performed a Fourier phase difference analysis between the two Doppler signals obtained for Hα and Ca II. The Doppler-shift measurements along PQ were interpolated to a fixed-interval (30 second) sampling for this purpose.

Figure 9 shows the phase difference between the Hα ($\delta\lambda = 0.35$ Å) and Ca II ($\delta\lambda = 0.15$ Å) Doppler velocities as function of frequency for four locations in the umbra (a), penumbra (b), and super-penumbra (c). The average phase difference in the three- and five-millihertz frequency bands are around 40° where cross-spectral power is significant. The

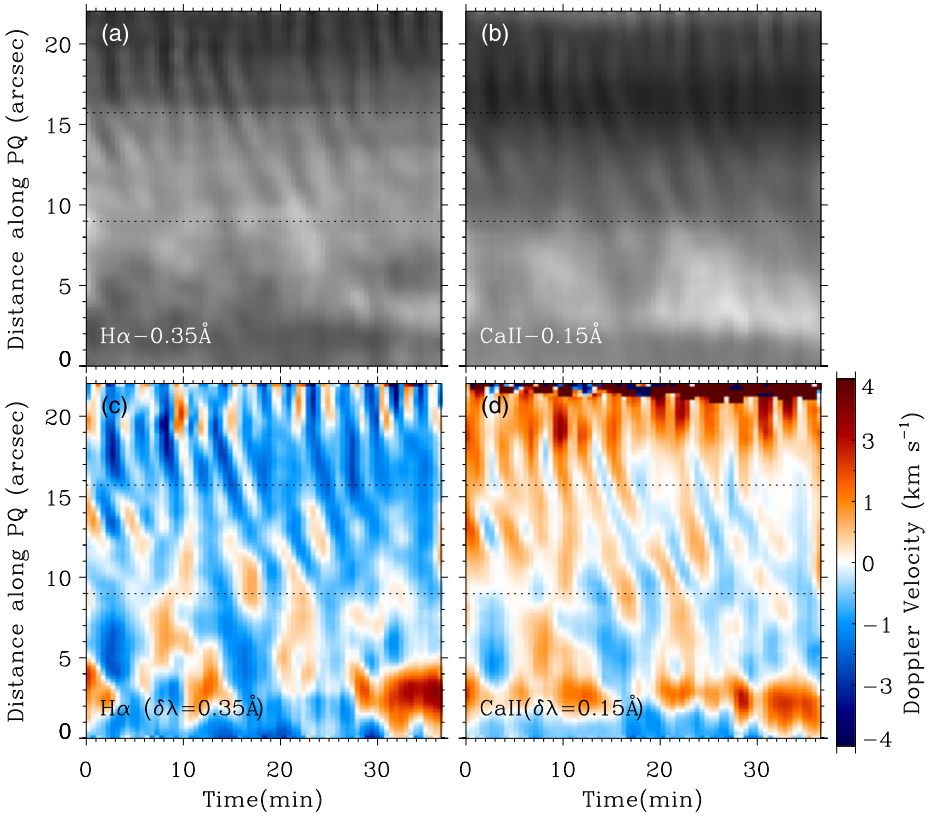

Figure 6 Space–time maps of intensity (upper row) and Doppler velocity (lower row), in Hα (left column) and Ca II (right column), along the reference line PQ (see Figure 1a). Dotted horizontal lines around 16″ and 9″ represent the approximate boundaries of the umbra and the penumbra, respectively.

phase difference shows that the UFs and RPWs are caused by upward-propagating MHD waves. The phase difference in the super-penumbral region is about 10° at lower frequency ≈ 1 mHz where significant power exists. This difference may be caused by noise and unequal sampling in the original data.

In order to ascertain the spatial variation in the oscillation power from umbra going outward, we have computed the root-mean-square (RMS) velocity [$v_{\rm rms}$] along the line PQ; results are shown in Figure 10. It is evident that $v_{\rm rms}$ is large in the umbra of both the Hα ($\delta\lambda = 0.35$ Å) and Ca II ($\delta\lambda = 0.15$ Å) and decreases (increases) in the penumbra (super-penumbra). In the inner umbra, Ca II $v_{\rm rms}$ for point Q rises considerably above the 2.1 km s^{-1} axis cutoff, which is caused by the combined effects of high Doppler velocities and large uncertainty in the Doppler-shift measurements. In the outer umbra, $v_{\rm rms}$ of Hα is larger than $v_{\rm rms}$ of Ca II. This may be due to the difference in formation height between the two spectral lines or some other difference in response. For example, Ca II may have higher opacity in cool post-shock gas than Hα (which has high opacity only in hot gas), so that Ca II is sensitive to cool post-shock downdrafts and Hα is not. The K_{2V}-like shock-grain pattern in Ca II may arise from shock interference along the line of sight. Towards P the LOS alignment is lost. The large $v_{\rm rms}$ in the umbra consists mostly of high-frequency power. The high-frequency components likely describe sawtooth shocks (see Figure 5).

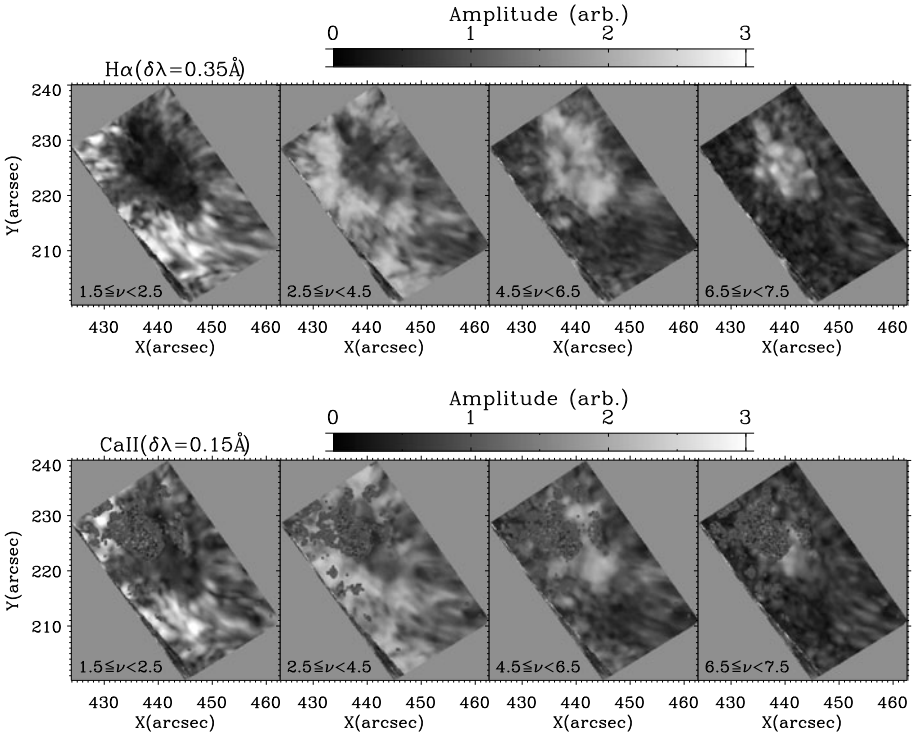

Figure 7 Average oscillation power maps in different frequency bands in mHz for the Hα ($\delta\lambda = 0.35$ Å) (upper) and Ca II ($\delta\lambda = 0.15$ Å) (lower).

Figure 11a shows the association in oscillation power and corresponding magnetic-field strength B from a rectangular area along line PQ of width of ten pixels. We noticed that the field strength of Figure 11a is not the same as in the HMI magnetogram in Figure 1. That indeed shows apparent polarity reversal in the penumbra from the line-of-sight projection. The mean oscillation power (see solid curves) in different frequency bands of both the Hα and Ca II lines shows a similar trend to the field strength [B]. At lower frequencies ($1.5 \leq \nu < 2.5$ mHz), the power is largest in areas with smaller B, which correspond to the regions of the outer penumbra, and rapidly decreases with B. In the frequency band $2.5 \leq \nu \leq 4.5$ mHz, the power initially increases up to $B \approx 700$ G and then decreases with B. In the frequency band $4.5 \leq \nu \leq 6.5$ mHz the oscillation power increases with B, becomes maximum around 1600 G, and then decreases rapidly. In the frequency band $6.5 \leq \nu \leq 7.5$ mHz most of the power is concentrated near the regions of very high B (> 1500 G), corresponding to the umbral region of the sunspot, while the power is nearly constant for the B range 300 – 1200 G.

To study the association between the oscillations and the field inclinations, we computed the inclination from the vertical to the surface using relation $\gamma = \cos^{-1}(B_r/|\mathbf{B}|)$, where B_r is the radial component of the magnetic field **B**. The uniform-shear method is used (Moon *et al.*, 2003) to resolve the 180° ambiguity in the azimuth angle.

Figure 11b shows the variation in the oscillation power with magnetic-field inclination [γ] corresponding to the top panel of magnetic-field strength [B]. It is evident that the trend in power with inclination angle is the reverse of that with the field strength. The average

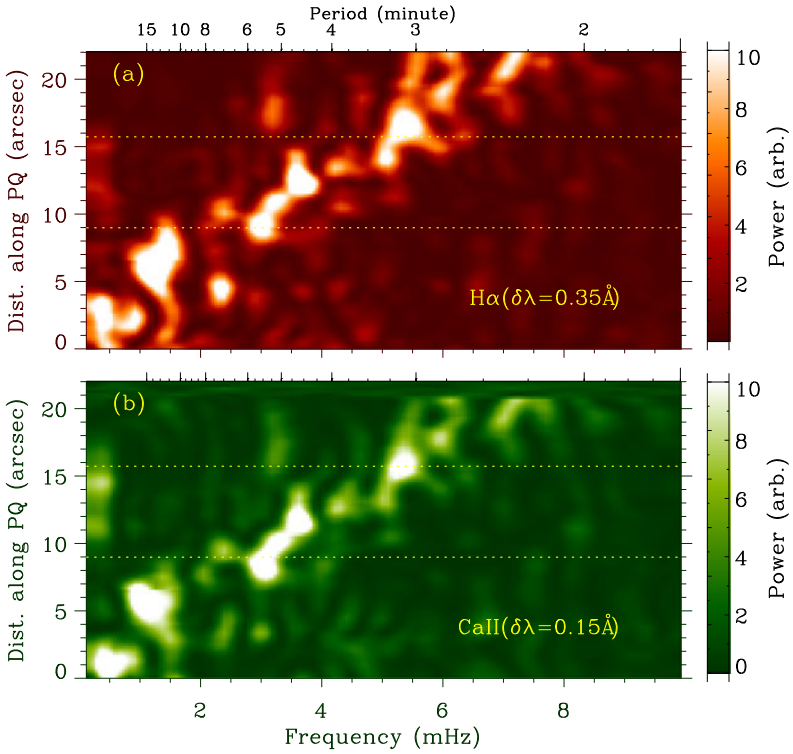

Figure 8 Oscillation-power maps along the line PQ (see Figure 1a) for the Doppler velocities of Hα ($\delta\lambda = 0.35$ Å) and Ca II ($\delta\lambda = 0.15$ Å). Dotted lines mark the boundaries as shown in Figure 6.

oscillation power (solid curves) in different frequency bands of both the Hα and Ca II lines behave similarly to the inclination except for smaller $\gamma \lessapprox 40$ at the high-frequency band $6.5 \leq \nu \leq 7.5$ mHz. This discrepancy in the Hα and Ca II lines arises due to UFs in Ca II. In the lower-frequency band ($1.5 \leq \nu < 2.5$ mHz), most power is concentrated at higher $\gamma > 80°$. The peak of the power distribution shifts toward lower inclination for higher-frequency bands. For instance in the frequency band $6.5 \leq \nu < 7.5$ mHz, most of the power is concentrated in the inclination region $10° - 30°$.

The opposite relation of inclination and field strength to the power is obvious from the magnetic-field distribution in the sunspot umbra; we have a strong field with small inclination. From the umbra outward the field strength increases while inclination decreases. Figure 11 shows that the oscillation power is associated both with the field strength and the inclination angle, but they behave differently in different frequency bands.

5. Summary and Conclusions

We studied the nature of running penumbral waves using Hα and Ca II Doppler images constructed with a bisector method from area scans with the FISS spectrometer. We found that the RPWs are easily seen in the intensity images constructed near the core, and their amplitude decays with wavelength from the line center outward. Also, their amplitude decreases from the umbra outward. These results are consistent with earlier results

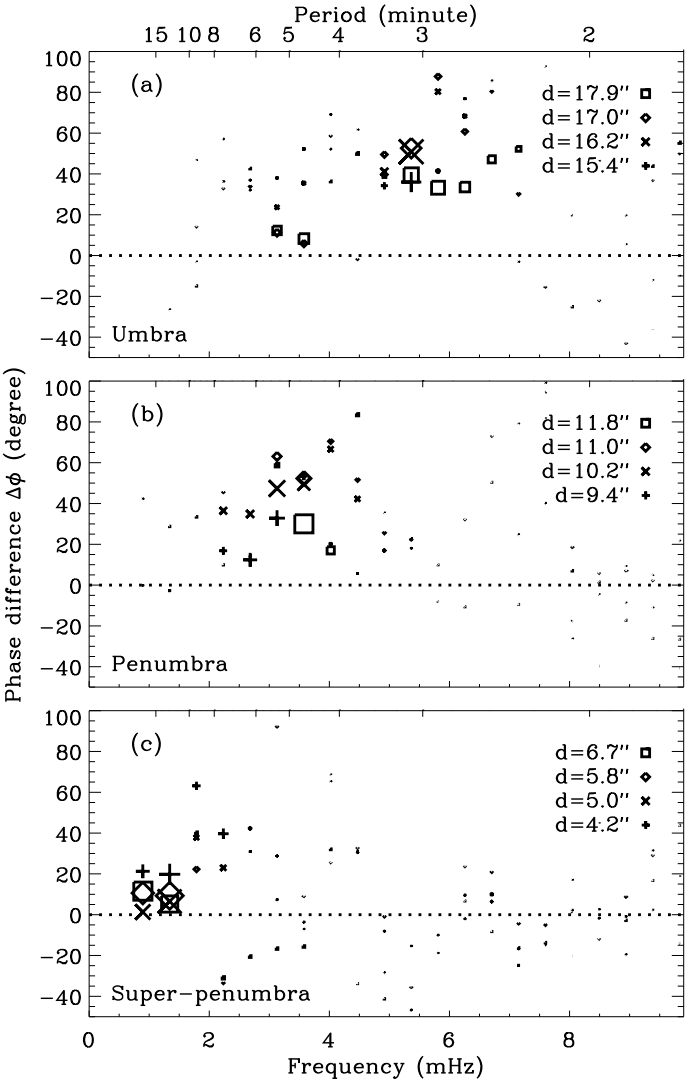

Figure 9 Phase difference [$\Delta\phi$] in Ca II ($\delta\lambda = 0.15$ Å) and Hα ($\delta\lambda = 0.35$ Å) Doppler velocities of: (a) umbra, (b) penumbra, and (c) super-penumbra, at four locations marked by symbols, square (□), diamond (◇), cross (×), and plus (+) along the reference line PQ (Figure 10a), where Ca II ($\delta\lambda = 0.15$ Å) is taken as leading. The distance [d] is measured from the point P along PQ. The symbol sizes represent the cross-spectral power between the two Doppler time series.

about the RPWs (Zirin and Stein, 1972; Christopoulou, Georgakilas, and Koutchmy, 2000; Tziotziou *et al.*, 2006). The running penumbral waves decay near the outer boundary of the penumbra.

We found that the chromosphere umbra of the sunspot shows large RMS velocity [$v_{\rm rms}$] in both spectral lines. From the umbra going outward, the $v_{\rm rms}$ gradually decreases, and there is no distinct boundary between the $v_{\rm rms}$ of the umbra and penumbra; however, $v_{\rm rms}$ has a minimum in the penumbral region. There is another interesting pattern seen in the $v_{\rm rms}$ of

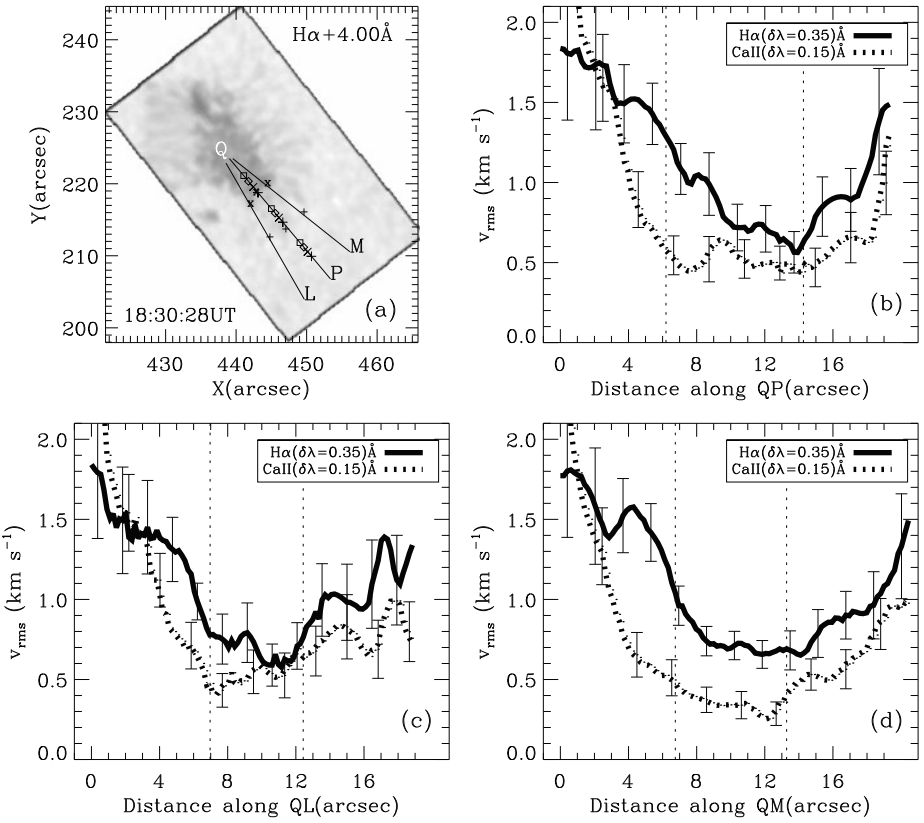

Figure 10 Variation in $v_{\rm rms}$ velocities of Hα ($\delta\lambda = 0.35$ Å) and Ca II ($\delta\lambda = 0.15$ Å) along the reference lines QN(b), QM(d), and QL(c) marked in the panel (a). Vertical dotted lines show the approximate umbral and penumbral boundaries marked by cross (×) and plus (+) symbols, respectively, over the solid curves in the panel (a). Other symbols (square–diamond–cross–plus "□ ⋄ ×+") in the umbra, penumbra, and super-penumbra of the sunspot mark the locations along the line PQ (same as in Figure 1a) for phase analysis in Figure 9.

Hα and Ca II lines; $v_{\rm rms}$ is smaller in Ca II than in Hα away from the umbral center. These results reveal that the Hα and Ca II lines are formed differently in the shocks that make up UFs. Furthermore $v_{\rm rms}$ is related to the oscillation power [power $\propto v_{\rm rms}^2$]. That is, we have larger power in the umbra than in penumbra; also, the power is larger in Hα than in Ca II.

Our time-series analysis of chromospheric Doppler maps shows high-frequency power in the umbra of both the spectral lines, Hα and Ca II, which is also evident from the $v_{\rm rms}$ distribution. This study shows that the total power gradually decreases with frequency from the umbra outward which confirms earlier reports (Tziotziou *et al.*, 2006; Nagashima *et al.*, 2007; Socas-Navarro *et al.*, 2009). The power maps indicate that this decrease is set by the high-frequency contribution. Our analysis of spectral observations shows that the high-frequency oscillations exist in the umbra of five-minute band. The observed power in the penumbral region shows strong peak in the three-minute band while the power is small at other frequencies.

The penumbral oscillations are regarded as a tail of the five-minute oscillations resulting in further dependence of the acoustic cutoff frequency on the magnetic-field inclination

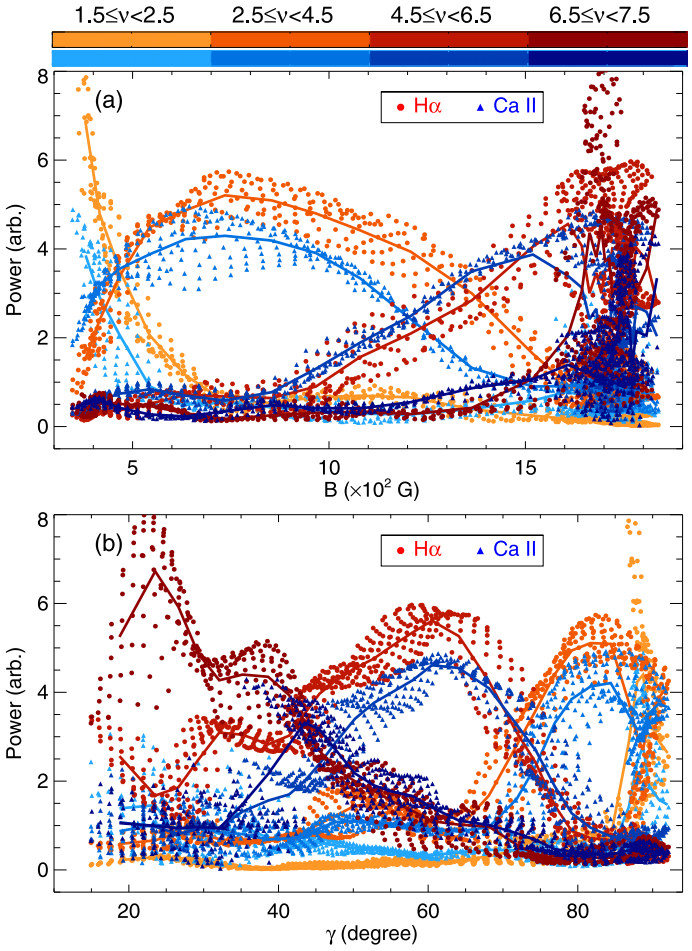

Figure 11 Scatter plots of oscillation power in different frequency bands (shown with different color gradients) against (a) magnetic field strength [B], and (b) magnetic-field inclination [γ], with mean curves (solid lines), for the rectangular area along line PQ of width ten pixels (see Figure 1a). Red and blue colors correspond to the Hα and Ca II lines, respectively.

(Cally, Bogdan, and Zweibel, 1994; De Pontieu, Erdélyi, and James, 2004). The oscillation power shows a strong relationship with the magnetic-field strength and angle of inclination. Our analysis showed that the peak oscillation frequency depends not only upon the inclination but also on the field strength.

Observations in Hα and Ca II bands demonstrated that the oscillations with frequencies around 5.0 mHz are dominant in the umbral and inner-penumbral regions, together with the presence of RPWs in the three-millihertz band.

We can summarize the above results as follows:

- Ca II showed reverse C-shaped bisectors at some locations within the sunspot.
- Bisector-measured Doppler velocity in Ca II is affected by umbral emission features.
- The amplitude of RPWs decreases with distance from the umbra outward and decays near the penumbral boundary.

- RPWs have much more blue than red in Hα and the reverse in Ca II.
- Peak-power frequency gradually increases from umbra to outward in both lines.
- In umbra and penumbra of the sunspot, the Hα and Ca II lines showed a phase difference of $\approx 40^\circ$ in the three- and five-minute oscillation bands.
- $v_{\rm rms}$ in the umbra is larger than in the penumbra of both lines. In the outer umbra, $v_{\rm rms}$ is larger in Hα than $v_{\rm rms}$ in Ca II.
- The oscillation power shows different relations with the magnetic-field strength and the inclination in different frequency bands.

We conclude that the main oscillation properties still suggest MHD waves propagating upward along fanning field, as in earlier studies, but with interesting as yet unexplained response differences between the two lines. The transformation of vertical oscillations into RPWs, at the boundary of umbra and penumbra, is an interesting feature, which requires further observations and theoretical studies to explain the wave phenomenon in the sunspot.

Acknowledgements HMI data are courtesy of NASA/SDO and the HMI science team. We thank the anonymous referee for their comments and important suggestions that helped to improve the quality of the manuscript. This work was support by the National Research Foundation of Korea (2011-0028102).

References

Bard, S., Carlsson, M.: 2010, *Astrophys. J.* **722**, 888. ADS:2010ApJ...722..888B. doi:10.1088/0004-637X/722/1/888.

Beckers, J.M., Tallant, P.E.: 1969, *Solar Phys.* **7**, 351. ADS:1969SoPh....7..351B. doi:10.1007/BF00146140.

Bhatnagar, A., Livingston, W.C., Harvey, J.W.: 1972, *Solar Phys.* **27**, 80. ADS:1972SoPh...27...80B. doi:10.1007/BF00151772.

Bloomfield, D.S., Lagg, A., Solanki, S.K.: 2007, *Astrophys. J.* **671**, 1005. ADS:2007ApJ...671.1005B. doi:10.1086/523266.

Cally, P.S., Bogdan, T.J., Zweibel, E.G.: 1994, *Astrophys. J.* **437**, 505. ADS:1994ApJ...437..505C. doi:10.1086/175014.

Cavallini, F., Ceppatelli, G., Righini, A., Alamanni, N.: 1986, *Astron. Astrophys.* **156**, 310. ADS:1986A&A...156..310C.

Chae, J., Park, H.M., Ahn, K., Yang, H., Park, Y.D., Nah, J., Jang, B.H., Cho, K.S., Cao, W., Goode, P.R.: 2012, *Solar Phys.* ADS:2012SoPh..tmp..248C. doi:10.1007/s11207-012-0147-x.

Christopoulou, E.B., Georgakilas, A.A., Koutchmy, S.: 2000, *Astron. Astrophys.* **354**, 305. ADS:2000A&A...354..305C.

De Pontieu, B., Erdélyi, R., James, S.P.: 2004, *Nature* **430**, 536. ADS:2004Natur.430..536D. doi:10.1038/nature02749.

Dravins, D., Lindegren, L., Nordlund, A.: 1981, *Astron. Astrophys.* **96**, 345. ADS:1981A&A....96..345D.

Giovanelli, R.G.: 1972, *Solar Phys.* **27**, 71. ADS:1972SoPh...27...71G. doi:10.1007/BF00151771.

Gray, D.F.: 1976, *The Observation and Analysis of Stellar Photospheres*, Wiley-Interscience, New York. ADS:1976oasp.book.....G.

Havnes, O.: 1970, *Solar Phys.* **13**, 323. ADS:1970SoPh...13..323H. doi:10.1007/BF00153554.

Keil, S.L., Yackovich, F.H.: 1981, *Solar Phys.* **69**, 213. ADS:1981SoPh...69..213K. doi:10.1007/BF00149989.

Kneer, F., Mattig, W., von Uexkuell, M.: 1981, *Astron. Astrophys.* **102**, 147. ADS:1981A&A...102..147K.

Lomb, N.R.: 1976, *Astrophys. Space Sci.* **39**, 447. ADS:1976Ap%26SS..39..447L. doi:10.1007/BF00648343.

Maurya, R.A.: 2010, PhD thesis, Udaipur Solar Observatory/Physical Research Laboratory, Mohan Lal Sukhadiya Univ., Udaipur, India. ADS:2010PhDT.....2M.

Maurya, R.A., Ambastha, A.: 2009, *Solar Phys.* **258**, 31. ADS:2009SoPh..258...31M. doi:10.1007/s11207-009-9397-7.

Maurya, R.A., Vemareddy, P., Ambastha, A.: 2012, *Astrophys. J.* **747**, 134. ADS:2012ApJ...747..134M. doi:10.1088/0004-637X/747/2/134.

Moon, Y., Wang, H., Spirock, T.J., Goode, P.R., Park, Y.D.: 2003, *Solar Phys.* **217**, 79. ADS:2003SoPh..217...79M.

Moore, R.L.: 1981, *Space Sci. Rev.* **28**, 387. ADS:1981SSRv...28..387M. doi:10.1007/BF00212601.

Nagashima, K., Sekii, T., Kosovichev, A.G., Shibahashi, H., Tsuneta, S., Ichimoto, K., Katsukawa, Y., Lites, B., Nagata, S., Shimizu, T., Shine, R.A., Suematsu, Y., Tarbell, T.D., Title, A.M.: 2007, *Publ. Astron. Soc. Japan* **59**, 631. ADS:2007PASJ...59S.631N.
Nye, A.H., Thomas, J.H.: 1974, *Solar Phys.* **38**, 399. ADS:1974SoPh...38..399N. doi:10.1007/BF00155077.
Nye, A.H., Thomas, J.H.: 1976, *Astrophys. J.* **204**, 582. ADS:1976ApJ...204..582N. doi:10.1086/154206.
Pearson, K.: 1901, *Phil. Mag.* **2**, 559.
Rees, D.E., López Ariste, A., Thatcher, J., Semel, M.: 2000, *Astron. Astrophys.* **355**, 759. ADS:2000A&A...355..759R.
Rouppe van der Voort, L.H.M., Rutten, R.J., Sütterlin, P., Sloover, P.J., Krijger, J.M.: 2003, *Astron. Astrophys.* **403**, 277. ADS:2003A&A...403..277R. doi:10.1051/0004-6361:20030237.
Scargle, J.D.: 1982, *Astrophys. J.* **263**, 835. ADS:1982ApJ...263..835S. doi:10.1086/160554.
Schou, J., Scherrer, P.H., Bush, R.I., Wachter, R., Couvidat, S., Rabello-Soares, M.C., Bogart, R.S., Hoeksema, J.T., Liu, Y., Duvall, T.L., Akin, D.J., Allard, B.A., Miles, J.W., Rairden, R., Shine, R.A., Tarbell, T.D., Title, A.M., Wolfson, C.J., Elmore, D.F., Norton, A.A., Tomczyk, S.: 2012, *Solar Phys.* **275**, 229. ADS:2012SoPh..275..229S. doi:10.1007/s11207-011-9842-2.
Slaughter, C.D., Wilson, A.M.: 1972, *Solar Phys.* **24**, 43. ADS:1972SoPh...24...43S. doi:10.1007/BF00231081.
Socas-Navarro, H., McIntosh, S.W., Centeno, R., de Wijn, A.G., Lites, B.W.: 2009, *Astrophys. J.* **696**, 1683. ADS:2009ApJ...696.1683S. doi:10.1088/0004-637X/696/2/1683.
Stebbins, R., Goode, P.R.: 1987, *Solar Phys.* **110**, 237. ADS:1987SoPh..110..237S. doi:10.1007/BF00206421.
Tziotziou, K., Tsiropoula, G., Mein, P.: 2002, *Astron. Astrophys.* **381**, 279. ADS:2002A&A...381..279T. doi:10.1051/0004-6361:20011419.
Tziotziou, K., Tsiropoula, G., Mein, N., Mein, P.: 2006, *Astron. Astrophys.* **456**, 689. ADS:2006A&A...456..689T. doi:10.1051/0004-6361:20064997.
Tziotziou, K., Tsiropoula, G., Mein, N., Mein, P.: 2007, *Astron. Astrophys.* **463**, 1153. ADS:2007A&A...463.1153T. doi:10.1051/0004-6361:20066412.
Uitenbroek, H.: 2006, *Astrophys. J.* **639**, 516. ADS:2006ApJ...639..516U. doi:10.1086/499220.
von Uexküll, M., Kneer, F., Mattig, W.: 1983, *Astron. Astrophys.* **123**, 263. ADS:1983A&A...123..263V.
Zhugzhda, I.D., Dzhalilov, N.S.: 1984, *Astron. Astrophys.* **133**, 333. ADS:1984A&A...133..333Z.
Zirin, H., Stein, A.: 1972, *Astrophys. J. Lett.* **178**, L85. ADS:1972ApJ...178L..85Z. doi:10.1086/181089.